Published in final edited form as:
J Biomed Nanotechnol. 2016 February ; 12(2): 296–307.

Imaging Intratumoral Nanoparticle Uptake after Combining Nanoembolization with Various Ablative Therapies in Hepatic VX2 Rabbit Tumors

Alda L Tam[1,*], **Marites P. Melancon**[1], **Mohamed Abdelsalam**[1], **Tomas Appleton Figueira**[1], **Katherine Dixon**[1], **Amanda McWatters**[1], **Min Zhou**[2], **Qian Huang**[2], **Osama Mawlawi**[3], **Kenneth Dunner Jr**[4], **Chun Li**[2], and **Sanjay Gupta**[1]

[1]Department of Interventional Radiology, The University of Texas, MD Anderson Cancer Center, Houston, TX, USA

[2]Department of Cancer Systems Imaging, The University of Texas, MD Anderson Cancer Center, Houston, TX, USA

[3]Department of Imaging Physics, The University of Texas, MD Anderson Cancer Center, Houston, TX, USA

[4]Department of Cancer Biology, The University of Texas, MD Anderson Cancer Center, Houston, TX, USA

Abstract

Combining image-guided therapy techniques for the treatment of liver cancers is a strategy that is being used to improve local tumor control rates. Here, we evaluate the intratumoral uptake of nanoparticles used in combination with radiofrequency ablation (RFA), irreversible electroporation (IRE), or laser induced thermal therapy (LITT). Eight rabbits with VX2 tumor in the liver underwent one of four treatments: (i) nanoembolization (NE) with radiolabeled, hollow gold nanoparticles loaded with doxorubicin (^{64}Cu-PEG-HAuNS-DOX); (ii) NE+RFA; (iii) NE+IRE; (iv) NE+LITT. Positron emission tomography/computed tomography (PET/CT) imaging was obtained 1-hr or 18-hrs after intervention. Tissue samples were collected for autoradiography and transmission electron microscopy (TEM) analysis. PET/CT imaging at 1-hr showed focal deposition of oil and nanoparticles in the tumor only after NE+RFA but at 18-hrs, all animals had focal accumulation of oil and nanoparticles in the tumor region. Autoradiograph analysis demonstrated nanoparticle deposition in the tumor and in the ablated tissues adjacent to the tumor when NE was combined with ablation. TEM results showed the intracellular uptake of nanoparticles in tumor only after NE+IRE. Nanoparticles demonstrated a structural change, suggesting direct interaction, potentially leading to drug release, only after NE+LITT. The findings demonstrate that a combined NE and ablation treatment technique for liver tumors is feasible, resulting in deposition of nanoparticles in and around the tumor. Depending on the ablative energy applied, different effects are seen on nanoparticle localization and structure. These

---

Correspondence: Alda Lui Tam, MD, Department of Interventional Radiology, Unit 1471, The University of Texas M.D. Anderson Cancer Center, PO Box 301402, Houston, Texas 77230-1402. Phone: 1 713 563 7920; Fax: 1 713 792 4098; alda.tam@mdanderson.org.

Disclosure: The authors report no conflicts of interest in this work.

effects should be considered when designing nanoparticles for use in combination with ablation technologies.

Keywords

tumor; radiofrequency ablation; laser induced thermal therapy; electroporation; nanoparticles; intracellular delivery; transmission electron microscopy

1. Introduction

The treatment of patients with primary or metastatic liver tumors is challenging. Hepatocellular carcinoma (HCC) is the third most common cause of cancer death,[1] and metastases to the liver, which often portends a grim prognosis, are common in solid malignancies such as melanoma,[2] breast,[3] and colorectal[4] cancer. The limited success and toxicity of systemic chemotherapy[5] and the constrained criteria for surgical resection, an option for only 5–20% of patients, provide the rationale for the use of techniques such as transarterial chemoembolization (TACE) or radiofrequency ablation (RFA) to provide locoregional therapy to patients with unresectable liver tumors.

Survival benefit after TACE[1,6] or RFA[7,8,9] has been demonstrated but when used in isolation, each technique is limited by the incomplete elimination of cancer cells, leading to local tumor recurrence and ultimately, treatment failure. To improve local control rates, multimodality (TACE and RFA) treatment strategies, capitalizing on synergistic effects, have been proposed.[10–13] Recent studies have demonstrated the efficacy of combined RFA and TACE with 5-year survival rates of 41% for lesions greater than 5 cm and 75% for lesions less than 5 cm[11,14] as compared to a 38% 5-year survival rate for lesions smaller than 5 cm treated with RFA alone.[15] There is clearly an emerging role for the multimodality treatment of liver tumors and studies are needed to establish the most effective strategies.

Newer ablation and embolization technologies, irreversible electroporation (IRE) and nanoembolization (NE), are currently being studied.[16–18] Electroporation involves the targeted delivery of electrical pulses to make cell membranes permeable, either temporarily (reversible electroporation, RE) or permanently (IRE). When compared to RFA or laser induced thermal therapy (LITT), electroporation has the unique potential to facilitate the intracellular delivery of therapeutic agents through the disruption of cellular membranes.[19–22] Nanoparticles have been used as a platform for the delivery of anti-neoplastic agents;[23,24] however, optimizing methods for efficient delivery to target sites remains a major challenge.[18] We hypothesize that nanoparticle distribution to the tumor will be different depending on the ablative technique that is used conjunction with NE and that intracellular uptake of nanoparticles will only be seen after NE+IRE. This proof of concept study uses functional imaging, autoradiography analysis and transmission electron microscopy (TEM) to investigate the intratumoral uptake of radiolabeled hollow gold nanoshells-loaded with doxorubicin (^{64}Cu-PEG-HAuNS-DOX) when combined with either RFA, IRE or LITT.

2. Experimental Section

2.1 Chemicals

Doxorubicin (Dox) was obtained from Ochem Incorporation (Des Plaines, IL). Methoxy-polyethylene glycol (PEG-SH, MW 5000), gold(III) chloride trihydrate, and phosphate-buffered saline (pH 7.4) were obtained from Sigma-Aldrich (St. Louis, MO). Sodium citrate dihydrate, trisodium citrate dihydrate (>99%), cobalt(II) chloride hexahydrate (99.99%), and sodium borohydride (99%) were obtained from Fisher Scientific (Pittsburgh, PA).

2.2 Nanoparticle Synthesis and Characterization

Dox@PEG-HAuNS (1:3:1 wt/wt, 20 optical density [OD]) was synthesized as described previously.[25] Briefly, 4.5 ml of sodium borohydride (1 M), 2.8 ml of sodium citrate (0.1 M), and 1.0 ml of cobalt chloride (0.4 M) were added to pre-deoxygenated deionized water with stirring to synthesize cobalt nanoparticle core template. Chloroauric acid was then added to the suspension of cobalt nanoparticles formed *in situ*, which reduced the gold ions to gold nanoparticles on the surface of the cobalt nanoparticles and oxidized cobalt to cobalt(II) ions. Any remaining cobalt was oxidized by air, resulting in the final product, HAuNS. The size of the HAuNS was determined using dynamic light scattering at a 90° scatter angle on a particle size analyzer (Brookhaven Instruments, Holtsville, NY). The amount of gold in the HAuNS was quantified using inductively coupled plasma mass spectroscopy (Galbraith, Knoxville, TN).

PEG-SH was then added to the HAuNS suspension under argon protection at room temperature. Excess PEG-SH was removed by subjecting the suspension to centrifugation and washing the residue with 1.5 mM sodium citrate (pH 6.5–7) twice. To load Dox onto the PEG-HAuNS, Dox was slowly added to the PEG-HAuNS suspension under stirring at room temperature (ratio is 1:3:1 w/w). After the mixture was stirred for 24 hrs, excess Dox was removed by subjecting the mixture to centrifugation and washing the supernatant with sodium citrate (1.5 mM) repeatedly until the supernatant became colorless. The amount of excess Dox in the supernatant was determined by spectrophotometry at 480 nm.

Radiolabeling of hollow gold nanoshells was accomplished by adding ^{64}Cu to the chelator, DOTA-LA (1,4,7,10-tetraazacyclododecane-1,4,7-tris(acetic acid)-10-acetic acid-N-(2-(2-(2-aminoethoxy)ethoxy)ethyl)-lipoic acid mono amide). DOTA-LA was synthesized according to previously published protocol.[26] Once the ^{64}Cu is attached to the chelator, ^{64}Cu-DOTA-LA was added to an aqueous solution of HAuNS-PEG-DOX (400 µL, ~2 x 10^{13} particles) at room temperature for 4 hours to produce ^{64}Cu-HAuNS-DOX. The radiolabeled nanoparticles were then purified by centrifugation at 8,000 rpm for 5 min and washed three times with PBS. The radiolabeling efficiency and the stability of labeled nanoparticles were analyzed using Instant thin layer chromatography (ITLC).

2.3 Animal Tumor Model

All experiments were approved by the Institutional Animal Care and Use Committee and were performed in accordance with institutional guidelines. The rabbits were maintained in facilities approved by the Association for Assessment and Accreditation of Laboratory

Animal Care and in accordance with current US Department of Agriculture, Department of Health and Human Services, and National Institutes of Health Regulations and Standards. Eight male, New Zealand white rabbits (weight range 2.8–3.4 kg) were used to complete the study. Our technique for tumor inoculation has been previously described in detail.[27] In brief, after the administration of intramuscular sedation and induction of surgical anesthesia, the abdomen was shaved and prepped for aseptic surgery. VX2 tumor was inoculated into the left lobe of the liver with 4mm chunks of freshly harvested VX2 tumor. A small puncture with an 11-blade scalpel was made into the left lobe of the liver and the tumor chunk was inserted, pressure was held, and the left lobe of the liver was replaced into the abdomen. The incision was closed in layers, and the animal was allowed to recover. The tumors were allowed to grow in the rabbits' livers for approximately 10–12 days.

2.4 In Vivo Experiments

Previous researchers[9,12] have shown that larger treatment volumes can be created when embolization is followed by ablation; therefore, nanoembolization was performed prior to IRE, RFA, or LITT. Doxorubicin has been chosen as the antineoplastic agent to be combined with the nanoparticles because it is the most active drug against HCC, producing tumor response rates of about 10–20%[28], and is the most common drug used in chemoembolization.[29]

Anesthesia was provided using isoflurane. Following the pre-treatment CT imaging, the right groin of the animal was shaved and prepared for aseptic surgery using alcohol-betadine scrub and betadine. A small incision was made and the right common femoral artery was isolated. A 4-French sheath was placed into the vessel through a small arteriotomy and sodium heparin (100 IU/kg) was given through the sheath. A microcatheter was introduced through the sheath and advanced into the common hepatic artery under fluoroscopic monitoring. Digital subtraction angiography of the celiac axis was performed by injecting 2–4 ml of meglumine-diatrizoate to document the vascular anatomy and tumor size. Then the catheter was advanced into the proper hepatic artery and positioned just above the origin of the gastroduodenal artery and nanoembolization (NE) using ^{64}Cu-PEG-HAuNS-DOX in combination with lipiodol oil (Guerbert LLC, France) was performed. A total volume of 1 mL (0.3 mL lipiodol oil; 0.5 mL ^{64}Cu-PEG-HAuNS-DOX; 0.2 mL contrast) was injected. Nanoembolization was terminated when the hepatic artery reached stasis.

Ablations were performed 2 minutes after NE in order to optimize the intracellular incorporation of the nanoparticles.[18] Ablation probes were placed using real-time ultrasound guidance. For the rabbit undergoing NE+RFA, a 17-gauge internally cooled electrode (Covidien, Dublin, Ireland) with a 2 cm active tip was placed into the center of the tumor. Ablation was performed using a 500-kHz RF generator (Valley Lab, Boulder, CO). RF energy was applied for 8 minutes with the generator output set to impedance mode. For the rabbit undergoing NE+IRE, two unipolar IRE electrodes, each with a 2 cm active tip, were positioned in parallel to encompass the liver tumor under ultrasound guidance. IRE ablation was performed using a pulse generator (AngioDynamics, Queensbury, NY) set at 90 pulses, 2700 V/cm, and 70 μs. For the rabbit undergoing NE+LITT, an 808-nm NIR 600-μm-diameter laser fiber (BioTex, Inc., Houston, TX) with a 2-cm long diffusing tip was inserted and LITT was performed at 2 W using a Diomed 15 laser system (New York, NY) for 3 minutes.

2.5 Positron Emission Tomography/Computed Tomography (PET/CT) Imaging

PET/CT was performed 1-hour or 18-hours after treatment to assess the distribution of the radiolabeled nanoparticles. PET/CT imaging was performed using a Discovery 610–64 PET/CT system (GE Healthcare). Helical CT scans covering the whole body of the rabbit were obtained using 120 kVp, 100 mAs, 13.5-mm/rotation table speed. Whole-body PET scans were then acquired with 3 minutes/bed position and 11 slice overlap. PET/CT images were reconstructed using standard vendor-provided reconstruction algorithms, and corrected for attenuation, scatter, dead time, and radioactive decay. To ensure that the measured injected dose was accurate in terms of activity measured by PET, we cross-calibrated the dose calibrator (CRC-15R; Capintec, Inc., Ramsey, N.J.) with the PET camera.[30] The whole-body reconstructed PET/CT data were then transferred in Digital Imaging and Communications in Medicine (DICOM) 3.0, part 10 file format to an AW workstation (GE Healthcare) for image analysis which consisted of drawing regions of interest around the tumor and normal liver parenchyma to determine the standard uptake value (SUV).

2.5 Tissue Analysis

All animals were euthanized with an overdose of beuthanasia-D (1.0 ml/10 lbs) (Schering-Plough Animal Health, Union, NJ). The tumor and the surrounding liver tissues were removed. The tissue sample was bisected and each half included tumor and surrounding liver. One half of the tumor and surrounding liver was placed into OTC media and frozen for atomic absorption analysis. The other half was placed into 2,3,5-triphenyl-2H-tetrazolium chloride (TTC) (Sigma, St. Louis, MO) which was used to stain for mitochondrial enzyme activity. This test is used to identify irreversible cellular injury during the initial time period following RFA[31,32] with viable liver staining red and unviable, ablated liver tissue remaining white, thus creating a definitive zone of demarcation between ablated and non-ablated liver tissue. Gross measurements of the tumor and ablation zones were obtained using a caliper. Multiple tissue samples from the tumor, ablation zone and peri-tumoral, non-ablated liver were obtained and then fixed for transmission electron microscopy (TEM) analysis. The remainder of the tissue was placed in formalin, embedded in paraffin, and cut into 5 μm slices for hematoxylin and eosin staining and autoradiograph. Autoradiography was performed by exposing sections of tumors to phosphorous screen film (an SR imaging plate) overnight at room temperature. The radioactive signal from ^{64}Cu was detected using a Fujifilm FLA-5100 imaging system (Stamford, CT).

2.6 Transmission Electron Microscopy (TEM) Analysis

Samples were fixed with a solution containing 3% glutaraldehyde plus 2% paraformaldehyde in 0.1 M cacodylate buffer, pH 7.3, then were washed and treated with 0.1% Millipore-filtered cacodylate buffered tannic acid, postfixed with 1% buffered osmium tetroxide for 30 min, and stained en bloc with 1% Millipore-filtered uranyl acetate. The samples were dehydrated in increasing concentrations of ethanol, infiltrated, and embedded in LX-112 medium. The samples were polymerized in a 60 C oven for 2 days. Ultrathin sections were cut in a Leica Ultracut microtome (Leica, Deerfield, IL), stained with uranyl acetate and lead citrate in a Leica EM Stainer, and examined in a JEM 1010 transmission electron microscope (JEOL, USA, Inc., Peabody, MA) at an accelerating voltage of 80 kV. Digital images were obtained using AMT Imaging System (Advanced Microscopy Techniques Corp, Danvers, MA).

3. Results

Figure 1A shows the schema of the structure of Dox@PEG-HAuNS. This HAuNS has maximum absorption at 808 nm, which is ideal for LITT using the 808 mn laser (Figure 1B), while free Dox had maximum absorption at 495 nm. When PEG-HAuNS is loaded with Dox, two peaks were observed: one at 495 nm, which is due to the presence of Dox, and at 808 nm, which is due to HAuNS (Figure 1B). The hydrodynamic volume of PEG-HAuNS was 42.5 nm as determined using the DLS, which was confirmed on TEM as shown in Figure 1C. Dox conjugation did not significantly change the size of the PEG-HAuNS. Dox loading efficiency was >98%. The concentration of Dox loaded onto 1-OD PEG-HAuNS was 0.0175 mg/ml. The ^{64}Cu labeling efficiency was >99% as measured using the i-TLC method. Figure 1D demonstrates that the ^{64}Cu labeling was also stable after 24 hours.

Analysis of the gross pathology yielded measurements from which tumor and ablation zone volumes were calculated (Table 1). Measurements were obtained after TTC staining, which renders dead cells white and viable cells red, to improve the accuracy of detecting ablation zone boundaries. Using the formula for calculating the volume of an ellipsoid, the tumor volumes calculated after TTC staining ranged from 0.45 to 1.26 cm^3. The ablation zone volumes for the animals euthanized after the 1-hr PET/CT were as follows: 1.01 cm^3 for NE +LITT, 3.46 cm^3 for NE+IRE, and 4.4 cm^3 for NE+RFA. Ablation zone volumes were found to be larger for the animals euthanized after the 18-hr PET/CT: 1.3 cm^3 for NE+LITT, 21.4 cm^3 for NE+IRE, and 10.1 cm^3 for NE+RFA. The ablation zones for the animals treated with LITT were smaller than when compared to the ablation zones created by the other ablation modalities but expected given the low laser power that was used. At the 1.5 to 2 W power range, heating is expected to extended 6–8 mm from the laser fiber, giving a more precise and controlled area of ablation.[27]

PET/CT imaging was performed 1-hr or 18-hrs after the intervention. Figure 2 shows the PET/CT images of the tumors injected with the radiolabeled nanoparticle in combination with various ablation techniques and quantification of the ratio of tumor-to-normal liver uptake for each animal is summarized in Table 1. Axial CT images of the liver clearly showed the presence of tumors in all the rabbits investigated. As shown in Figure 2, PET images obtained at the 1-hr time point showed that focal deposition of oil and colocalization of ^{64}Cu-PEG-HAuNS-DOX nanoparticles in the tumor was most intense after NE+RFA but also present after NE+LITT as both demonstrated increased tumor-to-normal liver uptake ratios. After NE alone or NE+IRE, the deposition of oil was located predominantly at the periphery of the tumors and there was diffuse distribution of radioactivity throughout the liver without focal accumulation in the tumor at 1 hr. The 18-hr imaging shows a selective accumulation of the nanoparticles in tumor in each of the different treatments. At the 1-hr imaging time point, the NE+LITT and NE+RFA animals demonstrated increased tumor-to-normal liver uptake ratios, calculated at 2 and 4.7, respectively but the ratios decreased to 1.5

(NE+LITT) and 1.4 (NE+RFA) at the 18-hr imaging time point. The opposite effect was noted in the NE and NE+IRE animals with the tumor-to-normal liver ratios increasing from 1.1 to 1.7 (NE) and 0.81 to 2.0 (NE+IRE) from the 1-hr to the 18-hr imaging time point.

Nanoparticle distribution on autoradiograph analysis (Figure 3) was noted around the periphery and in the tumor after NE+IRE, NE+LITT, and NE+RFA but seen predominantly in the periphery of the tumor after NE. After NE+IRE, while nanoparticles were identified in the tumor and adjacent ablated liver tissue, nanoparticles were also seen in the peri-tumoral, non-ablated liver. Minimal changes in distribution of the nanoparticles were noted between the two time points.

TEM was performed on tissues from the 1-hr animals and tissues were taken from three sampling points: the tumor, ablation zone, and peri-tumoral, non-ablated liver. TEM results showed the distribution of the nanoparticles at a cellular level after each therapeutic intervention. For NE alone, there was no intracellular uptake and the nanoparticles in the tumor were either in the extracellular space in between cells or in the blood vessels (Figure 4) in all three sampling locations. Similarly, nanoparticles were located in either the blood vessel or within the extracellular space after NE+RFA and NE+LITT (Figure 5 and 6, respectively). However, structural change of the nanoparticle, characterized by collapse and deformation with loss of the inherent spherical shape, was noted only after NE+LITT. Figure 7 showed that for NE+IRE, aside from extracellular localization of the nanoparticles, there was also internalization of the nanoparticles into the intracellular milieu in tumor cells, ablated liver cells, and peri-tumoral, non-ablated liver cells. The hollow interior of the nanoparticles are clearly shown Figure 7, and are located adjacent to the nucleus of the cell. No nanoparticles were observed to be within the nucleus of the cell.

4. Discussion

Local tumor recurrence is a problem that plagues minimally invasive interventional radiology techniques such as TACE and RFA. To overcome this issue for the treatment of liver tumors, recent clinical trials have incorporated the use of multi-modality therapy, such as TACE in combination with sorafenib,[33,34] TACE with radiation therapy,[35,36] or TACE with ablation,[37] in the hopes that by exploiting the synergy between treatments, the tumor-free margin can be enhanced. To support and optimize the design of translational clinical trials using emerging technologies, we undertook this proof of concept study to discern potential differences in mechanisms of action when combining a novel embolization agent, nanoparticles, with various ablative techniques that have been approved for human use. We chose to use the gold nanoshell (HAuNS) construct because of its known interactions with LITT as demonstrated pharmacokinetically and on magnetic resonance imaging.[24,27] Additional features like its small size (30–50 nm diameter), spherical shape, lack of a silica core and need for cytotoxic surfactant to ensure stability, make this nanoparticle construct attractive for molecular therapy[38,39] and suitable for this study.

We used three different techniques to assess nanoparticle distribution within the tumor: PET/CT, autoradiography, and TEM. Each method of assessment provided pieces of information on how the nanoparticles related with the ablation technique applied and the tumor tissue. PET/CT is a non-invasive method for evaluating nanoparticle distribution but with its resolution limited to the millimeter range, it offers information only about average drug distribution within the tumor compared with normal tissues.[40] Imaging with PET/CT at the 1-hr time point after intervention was designed to reflect the nanoparticle distribution as a function of the administration technique and imaging at the 18-hr time point was performed to provide a delayed assessment of nanoparticle localization. Autoradiography reflects the microregional assessment[41,42] of nanoparticle distribution within the tumor tissues but can be limited by tissue processing techniques and post-treatment tumor necrosis. However, neither of the aforementioned techniques can be used to verify the location of the nanoparticle at a cellular resolution. As the confirmation of intracellular localization and ability to study uptake rates for nanoparticles are important pieces of information if nanoparticles are going to be used as drug delivery vehicles.[43] We used TEM to image nanoparticle localization at the cellular level. Following the analysis of the tissues by all three methods, we found the distribution pattern of nanoparticles on PET/CT imaging, autoradiography, and TEM to be distinct and dependent on the treatment modality.

Following the NE intervention, focal localization of the nanoparticles into the tumor on PET/CT was not seen until the 18-hr imaging time point and was associated with a maximum tumor to liver SUV ratio of 1.7. Autoradiography results matched the findings on TEM both of which demonstrated the nanoparticles to be located within the blood vessels and interstitial space at the periphery of the tumor. Several authors have demonstrated that nanoembolization results in greater delivery of the nanoparticles to the tumor when compared to intravenous delivery methods.[17,18] However, as compared to Tian's study,[17] which demonstrated uniform intratumoral uptake and increased tumor to liver ratios at both the 1-hour and 24-hour time points, our study showed predominantly peripheral uptake and increased tumor to liver ratio only on the delayed (18-hour) imaging. First, the peripheral localization of the nanoparticles may be related to the use of VX2 as the tumor model. VX2 tumors have a high rate of spontaneous necrosis[44,45] and it is possible that our tumors were highly necrotic prior to treatment. This would have resulted in a tumor with a largely necrotic and hypovascular center with the viable tumor tissue being concentrated in the periphery, accounting for why our nanoparticles were preferentially localized to that area. Second, the increased intratumoral uptake over time resulting in high tumor to liver ratio at the 18-hour time point seen in our study may be attributed to extravasation of recirculating NP from the blood pool through the abnormal tumor blood vessels that are known to have increased permeability as compared to normal liver blood vessels. Although the study by Tian et al.[17] suggested the possibility of internalization of the NP at 24 hours based on combined fluorescence and dark-field microphotography, TEM evaluation in our study did not show presence of NP inside the cells at the 18-hour time point. The accepted theory is that cellular internationalization of gold nanoparticles depends primarily on endocytosis[43] which does not occur rapidly.[22] In vitro experiments have demonstrated that metallic nanoparticles have to be incubated with cells for 20 hours or more before surface-enhanced Raman scattering experiments.[22] Because our analysis was not carried out beyond 18-hours, it is possible that our experimental time frame was too short to fully capture the mechanism of action of the intra-arterially delivered nanoparticles.

When considering nanoembolization as a stand-alone procedure, the approach to optimizing tumoral uptake relies primarily on modification of the nanoparticle design as nanoparticle size, shape, and charge can affect rates of internalization.[23,43] For spherical gold nanoparticles, particles that are within the 40–50 nm range, such as the ones used in this study, are the most effectively internalized via endocytosis[46] whereas for elongated nanoparticles, those with a positive charge can be internalized faster and more efficiently.[47] However, improvements in nanoconstruct design alone are not sufficient to surmount the issue of subtherapeutic dosing and additional nanoparticle delivery strategies are still needed to overcome tumor tissue heterogeneity and vascular perfusion variations to facilitate intratumoral nanoparticle deposition. The improvement in intratumoral nanoparticle uptake was seen on PET/CT imaging when combined NE with RFA or LITT. It is known that embolization before RFA can increase efficacy of treatment.[10] By decreasing tumor blood flow and reducing the heat sink effect, embolization prior to RFA can increase tumor heating and coagulation,[49,]50 resulting in a larger zone of ablation.[10] Additionally, the tissues at the periphery of the tumor subjected to sublethal hypothermic temperatures experience an increase in blood flow[50,51] and this hyperemia is thought to further increase drug deposition[52] and potentially enhance the maximal coagulation diameter following RFA.[53] We hypothesize that the mechanical effects of tissue destruction following RFA served to trap the nanoparticles already in the tumor and that the hyperemia induced in the tumor periphery allowed for additional nanoparticle to flow in and be deposited into the tumor, thus resulting in the increased uptake seen on PET/CT. Nanoparticle deposition in the tumor and tumor periphery after NE+RFA was confirmed on autoradiography but no cellular internalization or structural change of the nanoparticle was noted on TEM. RFA appears to be powerful adjunct to facilitate nanoparticle delivery into the tumor but future work should take into consideration mechanisms to ensure drug release.

Similarly, nanoembolization prior to LITT has been shown to be more effective with the enhanced antitumor activity thought to be a result of both the cytotoxic effect of paclitaxel and the photothermal effect mediated by the hollow gold nanospheres.[27] The most striking finding in the NE+LITT animals was the structural deformation of the nanoparticle seen on TEM, providing visualization of the effects of the laser interaction with the nanoparticles. Nanoparticles found in peri-tumoral, non-ablated liver parenchyma that were not exposed to the laser energy demonstrated no structural changes. While previous authors have demonstrated drug release using the hollow gold nanoshell construct and LITT[25,27] neither study used TEM and therefore were unable to image any changes in structure to their nanoparticles. Conversely, our study did not quantify drug release but the TEM images showing breakdown of individual nanoparticles along with the data previously described[25,27] suggest that doxorubicin was released successfully within the tumor. LITT has a known and validated interaction with gold nanostructures resulting in photothermal ablation and the ability to release cytotoxic agents. However, current laser fibers deliver energy focally and the heat generated does not extend very far from the fiber itself.[27] We saw evidence of this limitation on our gross measurements after NE+LITT as there was no well defined ablation zone around the tumor as was seen after NE+RFA and NE+IRE. Additional work is needed in order to optimize LITT settings to permit the treatment of larger tumors with nanoparticles.

The effects of electroporation on cell membrane permeability have been studied extensively[21,54] and the technology has been applied as a physical method for the delivery of therapeutic molecules, including DNA, into cells.[20,22] Similar to the vascular changes seen after RFA, tumors subjected to electroporation undergo changes in tumor blood flow.[55] It has been hypothesized that after electroporation a "vascular lock" phenomenon occurs in the tissues and is caused by a reflexive constriction of resistance vessels leading to the electroporated area and a phase of reduced intravascular pressure due to the increased permeability of the cell membranes.[55] The net effect of the vascular lock phenomenon results in the promotion of drug retention provided that the drug is present in the tumor tissues before electroporation.[54] Given these vascular effects, we expected to see better focal localization of the nanoparticles to the tumor at the 1-hr time point on PET/CT following NE +IRE. Instead, we saw more tumoral uptake on the delayed images where the tumor-to-normal liver SUV ratio was 2 which suggests that more than 1-hr is required to complete the process of nanoparticle internalization into the tumor. Clearly, dynamic imaging would be of great help to determine the rate of nanoparticle uptake following IRE as authors have suggested that electroporation's advantage as an ablation modality is its ability to speed up the cellular internalization of molecules.[19,22] Mouli et al.[18] combined NE+IRE in a rabbit hepatic VX2 tumor model and demonstrated increased nanoparticle uptake in the tumor core and tumor periphery without significant difference in delivery to healthy liver tissue.[18] They hypothesized that the combination therapy with electroporation would result in a rapid influx of nanoparticles into the cells that would not be dependent on cellular uptake mechanisms or the cell cycle, however, nanoparticle localization was determined by high resolution 7T MRI without direct evidence of intracellular localization.[18] Our TEM results support our initial hypothesis that NE+IRE would be the only combination therapy to demonstrate cellular internalization and our data show nanoparticles in the cytoplasm of tumor cells, ablated liver cells and peri-tumoral, non-ablated liver cells at both time points. This supports the findings of others who have demonstrated that electroporation can shorten the time frame for particle internalization.[19,22] However, the lack of structural deformity of the nanoparticles suggests that doxorubicin was not released and provides a direction for further investigation. Studies to optimize the drug release mechanism of the nanoparticle that could be used with electroporation could make it a more powerful drug delivery and treatment platform for solid tumors.

The study is not without limitations as it was designed to explore only the effects on nanoparticle localization after ablative therapy rather than therapeutic efficacy or toxicity. First, the VX2 tumor model in the rabbit can have a highly variable growth rate and a significant amount of spontaneous necrosis,[44,45] both of which could have affected the blood flow, delivery, and distribution of nanoparticles within the tumors. Second, the number of study animals is very small allowing for descriptive results without a statistical comparison. Ideally, these results would have to be replicated in a larger set of animals and correlated to the antitumor efficacy of the treatment modalities on histology. Third, similar to the work by Tian et al.,[17] the optimal interval between nanoparticle injection and peak tumor uptake was not defined. This study shows that significant uptake can happen between 1 h and 18 h, suggesting that functional imaging could be used to further evaluate pharmacokinetics for optimizing treatment planning. Finally, future studies should incorporate a quantification of the drug content within the tissues to evaluate for the successful release of the chemotherapeutic agent from the nanoparticle carrier.

5. Conclusion

This proof of concept, imaging study demonstrates that nanoparticles interact with ablative techniques and the interactions are different depending on the ablation modality. Some ablation techniques can help with tumor retention of nanoparticles: nanoparticles are incorporated into cells only after IRE, and demonstrate structural deformation, suggesting drug release, only after LITT. These types of interactions should be considered when designing nanoparticles for therapeutic use in combination with ablation technologies. Lastly, TEM findings demonstrate that a combined nanoembolization and IRE ablation treatment technique results in the intracellular deposition of nanoparticles into tumor and surrounding peri-tumoral, non-ablated liver cells, raising the possibility of achieving an ablation zone without gross or microscopic tumor remnants.

Acknowledgments

This work was supported in part by grants from the Radiologic Society of North America (2013 Research Seed Grant), the John S. Dunn Foundation, the Levit Family Endowment, and the MD Anderson Cancer Center Core Grant CA16672 High Resolution Electron Microscopy Facility.

References

1. Llovet JM, Bruix J. Novel advancements in the management of hepatocellular carcinoma in 2008. J Hepatol. 2008; 48(Suppl 1):S20–37. [PubMed: 18304676]
2. Gupta S, Bedikian AY, Ahrar J, Ensor J, Ahrar K, Madoff DC, Wallace MJ, Murthy R, Tam A, Hwu P. Hepatic artery chemoembolization in patients with ocular melanoma metastatic to the liver: response, survival, and prognostic factors. Am J Clin Oncol. 2010; 33:474–480. [PubMed: 19935383]
3. Wyld L, Gutteridge E, Pinder SE, James JJ, Chan SY, Cheung KL, Robertson JF, Evans AJ. Prognostic factors for patients with hepatic metastases from breast cancer. Br J Cancer. 2003; 89:284–290. [PubMed: 12865918]
4. Rabeneck L, El-Serag HB, Davila JA, Sandler RS. Outcomes of colorectal cancer in the United States:no change in survival (1986–1997). Am J Gastroenterol. 2003; 98:471–477. [PubMed: 12591071]
5. Mathurin P, Rixe O, Carbonell N, Bernard B, Cluzel P, Bellin MF, Khayat D, Opolon P, Poynard T. Review article: Overview of medical treatments in unresectable hepatocellular carcinoma—an impossible meta-analysis? Aliment Pharmacol Ther. 1998; 12:111–126.
6. Lo CM, Ngan H, Tso WK, Liu CL, Lam CM, Poon RT, Fan ST, Wong J. Randomized controlled trial of transarterial lipiodol chemoembolization for unresectable hepatocellular carcinoma. Hepatology. 2002; 35:1164–1171. [PubMed: 11981766]
7. Lencioni R, Crocetti L. A critical appraisal of the literature on local ablative therapies for hepatocellular carcinoma. Clin Liver Dis. 2005; 9:301–314. [PubMed: 15831275]
8. Galandi D, Antes G. Radiofrequency thermal ablation versus other interventions for hepatocellular carcinoma. Cochrane Database Syst Rev. 2004:CD003046. [PubMed: 15106188]
9. Liu PH, Lee YH, Hsu CY, Huang YH, Chiou YY, Lin HC, Huo TI. Survival advantage of radiofrequency ablation over transaterial chemoembolization for patients with hepatocellular carcinoma and good performance status within the Milan criteria. Ann Surg Oncol. Jun 6.2014 Epub ahead of print.

10. Mostafa EM, Ganguli S, Faintuch S, Mertyna P, Goldberg SN. Optimal strategies for combining transvascular arterial chemoembolization and radiofrequency ablation in rabbit VX2 hepatic tumors. J Vasc Interv Radiol. 2008; 19:1740–1748. [PubMed: 18951042]
11. Yamakado K, Nakatsuka A, Takaki H, Yokoi H, Usui M, Sakurai H, Isaji S, Shiraki K, Fuke H, Uemoto S, Takeda K. Early-stage hepatocellular carcinoma: radiofrequency ablation combined with chemoembolization versus hepatectomy. Radiology. 2008; 247:260–266. [PubMed: 18305190]
12. Tateishi R, Shiina S, Teratani T, Obi S, Sato S, Koike Y, Fujishima T, Yoshida H, Kawabe T, Omata M. Percutaneous radiofrequency ablation for hepatocellular carcinoma: an analysis of 1000 cases. Cancer. 2005; 103:1201–1209. [PubMed: 15690326]
13. Ahmed M, Goldberg SN. Combination radiofrequency thermal ablation and adjuvant IV liposomal doxorubicin increases tissue coagulation and intra-tumoral drug accumulation. Int J Hyperthermia. 2004; 20:781–802. [PubMed: 15675672]
14. Takaki H, Yamakado K, Uraki J, Nakatsuka A, Fuke H, Yamamoto N, Shiraki K, Yamada T, Takeda K. Radiofrequency ablation combined with chemoembolization for the treatment of hepatocellular carcinomas larger than 5 cm. J Vasc Interv Radiol. 2009; 20:217–224. [PubMed: 19097810]
15. Poon RT, Fan ST, Tsang FH, Wong J. Locoregional therapies for hepatocellular carcinoma: a critical review from the surgeon's perspective. Ann Surg. 2002; 235:466–486. [PubMed: 11923602]
16. Davalos RV, Mir LM, Rubinsky B. Tissue ablation with irreversible electroporation. Ann Biomed Eng. 2005; 33:223–231. [PubMed: 15771276]
17. Tian M, Lu W, Zhang R, Xiong C, Ensor J, Nazario J, Jackson J, Shaw C, Dixon KA, Miller J, Wright K, Li C, Gupta S. Tumor uptake of hollow gold nanospheres after intravenous and intra-arterial injection: PET/CT study in a rabbit VX2 liver cancer model. Mol Imaging Biol. 2013; 15:614–624. [PubMed: 23608932]
18. Mouli SK, Tyler P, McDevitt JL, Eifler AC, Guo Y, Nicolai J, Lewandowski RJ, Li W, Procissi D, Ryu RK, Wang YA, Salem R, Larson AC, Omary RA. Image-guided local delivery strategies enhance therapeutic nanoparticle uptake in solid tumors. ACS Nano. 2013; 7:7724–7733. [PubMed: 23952712]
19. Au JT, Wong J, Mittra A, Carpenter S, Haddad D, Carson J, Jayaraman S, Monette S, Solomon SB, Ezell P, Fong Y. Irreversible electroporation is a surgical ablation technique that enhances gene transfer. Surgery. 2011; 150:474–479. [PubMed: 21878233]
20. Rols MP. Electropermeabilization, a physical method for the delivery of therapeutic molecules into cells. Biochim Biophys Acta. 2006; 1758:423–428. [PubMed: 16483538]
21. Teissie J, Escoffre JM, Paganin A, Chabot S, Bellard E, Wasungu L, Rols MP, Golzio M. Drug delivery by electropulsation: recent developments in oncology. Int J Pharm. 2012; 423:306.
22. Lin J, Chen R, Feng S, Li Y, Huang Z, Xie S, Yu Y, Cheng M, Zeng H. Rapid delivery of silver nanoparticles into living cells by electroporation for surface-enhanced Raman spectroscopy. Biosense Bioelectron. 2009; 25:388–394.
23. Jain TK, Morales MA, Sahoo SK, Leslie-Pelecky DL, Labhasetwar V. Iron oxide nanoparticles for sustained delivery of anticancer agents. Mol Pharm. 2005; 2:194–205. [PubMed: 15934780]
24. Lee HJ, Liu Y, Zhao J, Zhou M, Bouchard RR, Mitcham T, Wallace MJ, Stafford RJ, Li C, Gupta S, Melancon MP. In vitro and in vivo mapping of drug release after laser ablation thermal therapy with doxorubicin-loaded hollow gold nanoshells using fluorescence and photoacoustic imaging. J Control Release. 2013; 172:152–158. [PubMed: 23920038]
25. You, Zhang R, Zhang G, Zhong M, Liu Y, Van Pelt CS, Liang D, Wei WJ, Sood AK, Li C. Photothermal-chemotherapy with doxorubicin-loaded hollow gold nanospheres: A platform for near-infrared light-trigged drug release. J Control Release. 2012; 158:319–328. [PubMed: 22063003]
26. Lu W, Zhang G, Zhang R, Flores LG 2nd, Huang Q, Gelovani JG, Li C. Tumor site specific silencing of NF-kappaB p65 by targeted hollow gold nanosphere-mediated photothermal transfection. Cancer Res. 2010; 70:3177–3188. [PubMed: 20388791]

27. Gupta S, Stafford RJ, Javadi S, Ozkan E, Ensor JE, Wright KC, Elliot AM, Jian Y, Serda RE, Dixon KA, Miller JJ, Klump S, Wallace MJ, Li C. Effects of near-infrared laser irradiation of biodegradable microspheres containing hollow gold nanospheres and paclitaxel administered intraarterially in a rabbit liver tumor model. J Vasc Interv Radiol. 2012; 23:553–561. [PubMed: 22341633]
28. Mabed M, Esmaeel M, El-Khodary T, Awad M, Amer T. A randomized controlled trial of transcatheter arterial chemoembolization with lipiodol, doxorubicin and cisplatin versus intravenous doxorubicin for patients with unresectable hepatocellular carcinoma. Eur J Cancer Care. 2009; 18:492–499.
29. Pleguezuelo M, Marelli L, Misseri M, Germani G, Calvaruso V, Xiruochakis E, Manousou P, Burroughs AK. TACE versus TAE as therapy for hepatocellular carcinoma. Expert Rev Anticancer Ther. 2008; 8:1623–1641. [PubMed: 18925854]
30. Tian M, Ogawa K, Wendt R, Mukhopadhyay U, Balatoni J, Fukumitsu N, Uthamanthil R, Borne A, Brammer D, Jackson J, Mawlawi O, Yang B, Alauddin MM, Gelovani JG. Whole-body biodistribution kinetics, metabolism, and radiation dosimetry estimates of 18F-PEG6-IPQA in nonhuman primates. J Nucl Med. 2011; 52:934–941. [PubMed: 21571803]
31. Goldberg SN, Saldinger PF, Stuart K, Gazelle GS, Huertas JC, Kruskal JB. Percutaneous tumor ablation: increased coagulation by combining radiofrequency ablation and ethanol instillation in a rat breast tumor model. Radiology. 2000; 217:827–831. [PubMed: 11110950]
32. Goldberg SN, Saldinger PF, Stuart K, Gazelle GS, Huertas JC, Jacobs T, Kruskal JB. Percutaneous tumor ablation: increased necrosis with combined radiofrequency ablation and intratumoral doxorubicin injection in a rat breast tumor model. Radiology. 2001; 220:420–427. [PubMed: 11477246]
33. Zhang L, Hu P, Chen X, Bie P. Transarterial chemoembolization (TACE) plus sorafenib versus TACE for intermediate or advanced stage hepatocellular carcinoma: a meta-analysis. PLoS One. 2014; 19:e100305. eCollection 2014.
34. Fu Q, Zhang QH, Bai XL, Hu QD, Su W, Chen YW, Su RG, Liang TB. Sorafenib enhances effects of transarterial chemoembolization for hepatocellular carcinoma: a systematic review and meta-analysis. J Cancer Res Clin Oncol. 2014; 140:1429–1440. [PubMed: 24770582]
35. Honda Y, Kimura T, Aikata H, Nakahara T, Naeshiro N, Tanaka M, Miyahi D, Nagaoki Y, Kawaoka T, Takaki S, Hiramatsu A, Waki K, Ishikawa M, Kakizawa H, Kenjo M, Awai K, Nagata Y, Chayama K. Pilot study of sterotactic body radiation therapy combined with transcatheter arterial chemoembolization for small hepatocellular carcinoma. Hepatogastroenterology. 2014; 61:31–36. [PubMed: 24895789]
36. Kim SW, Oh D, Park HC, Lim do H, Shin SW, Cho SK, Gwak GY, Choi MS, Paik YH, Paik SW. Transcatheter arterial chemoembolization and radiation therapy for treatment-naïve patients with locally advanced hepatocellular carcinoma. Radiat Oncol J. 2014; 32:14–22. [PubMed: 24724047]
37. Liu Z, Gao F, Yang G, Singh S, Lu M, Zhang T, Zhong Z, Zhang F, Tang R. Combination of radiofrequency ablation with transarterial chemoembolization for hepatocellular carcinoma: an up-to-date meta-analysis. Tumour Biol. 2014; 35:7407–7413. [PubMed: 24777334]
38. Lu W, Xiong C, Zhang G, Huang Q, Zhang R, Zhang JZ, Li C. Targeted photothermal ablation of murine melanomas with melanocyte-stimulating hormone analog-conjugated hollow gold nanospheres. Clin Cancer Res. 2009; 15:876–886. [PubMed: 19188158]
39. Melancon MP, Lu W, Yang Z, Zhang R, Cheng Z, Elliot AM, Stafford J, Olson T, Zhang JZ, Li C. In vitro and in vivo targeting of hollow gold nanoshells directed at epidermal growth factor receptor for photothermal ablation therapy. Mol Cancer Ther. 2008; 7:1730–1739. [PubMed: 18566244]
40. Minchinton AI, Tannock IF. Drug penetration in solid tumors. Nat Rev Cancer. 2006; 6:583–592. [PubMed: 16862189]
41. Kuh HJ, Jang SH, Wientjes MG, Weaver JR, Au JL. Determinants of paclitaxel penetration and accumulation in human solid tumor. J Pharmacol Exp Ther. 1999; 290:871–880. [PubMed: 10411604]
42. Jang SH, Wientjes MG, Lu D, Au JL. Drug delivery and transport to solid tumors. Pharm Res. 2003; 20:1337–1350. [PubMed: 14567626]

43. Sobhan MA, Sreenivasa VKA, Withford MJ, Goldys EM. Non-specific internalization of laser ablated pure gold nanoparticles in pancreatic tumor cell. Coloids Surf B Biointerfaces. 2012; 92:190–195.

44. Parvinian A, Casadaban LC, Gaba RC. Development, growth propagation, and angiographic utilization of the rabbit VX2 model of liver cancer: a pictorial primer and "how to" guide. Diagn Interv Radiol. 2014; 20:225–240.

45. Miao Y, Ni Y, Mulier S, Yu J, De Wever I, Penninckx F, Baert AL, Marchal G. Treatment of VX2 liver tumor in rabbits with "wet" electrode mediated radiofrequency ablation. Eur Radiol. 2000; 10:188–194. [PubMed: 10663742]

46. Jiang W, Kim BY, Rutka JT, Chan WC. Nanoparticle-mediated cellular response is size dependent. Nat Nanotechnol. 2008; 3:145–150. [PubMed: 18654486]

47. Gratton SE, Ropp PA, Pohlhaus PD, Luft JC, Madden VJ, Napier ME, DeSimone JM. The effect of particle design on cellular internalization pathways. Proc Natl Acad Sci USA. 2008; 105:11613–11618. [PubMed: 18697944]

48. Brown DB. Concepts, considerations, and concerns on the cutting edge of radiofrequency ablation. J Vasc Interv Radiol. 2005; 16:597–613. [PubMed: 15872314]

49. Lu DS, Raman SS, Vodopich DJ, Wang M, Sayre J, Lassman C. Effect of vessel size on creation of hepatic radiofrequency lesions in pigs: assessment of the "heat sink" effect. Am J Roentgenol. 2002; 178:47–51. [PubMed: 11756085]

50. Dudar TE, Jain RK. Differential response of normal and tumor microcirculation to hyperthermia. Cancer Res. 1984; 44:605–612. [PubMed: 6692365]

51. Kruskal JB, Oliver B, Huertas JC, Goldberg SN. Dynamic intrahepatic flow and cellular alterations during radiofrequency ablation of liver tumors in mice. J Vasc Interv Radiol. 2001; 12:1193–1201. [PubMed: 11585886]

52. Monsky WL, Goldberg SN, Huertas JC, Torchillin VP, Kruskal JB. Radiofrequency ablation increase intratumoral liposomal doxorubicin accumulation resulting in a synergistic increase in efficacy in animal breast tumor model (abstr). Radiology. 2000; 217(P):571.

53. Goldberg SN, Girnan GD, Lukyanov AN, Ahmed M, Monsky WL, Gazelle GS, Huertas JC, Stuart KE, Jacobs T, Torchillin VP, Halpern EF, Kruskal JB. Percutaneous tumor ablation: increased necrosis with combined radiofrequency ablation and intravenous liposomal doxorubicin in a rat breast tumor model. Radiology. 2002; 222:797–804. [PubMed: 11867804]

54. Gehl J. Electroporation: theory and methods, perspectives for drug delivery, gene therapy and research. Acta Physiol Scan. 2003; 177:437–447.

55. Sersa G, Cemazar M, Parkins CS, Chaplin DJ. Tumor blood flow changes induced by application of electric pulses. Eur J Cancer. 1999; 35:672–677. [PubMed: 10492645]

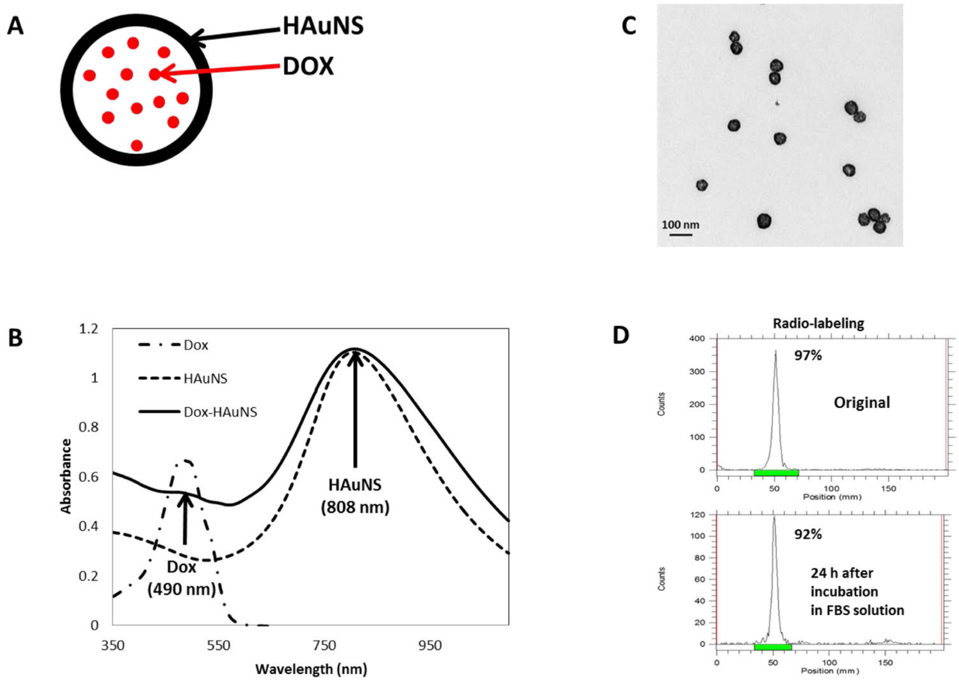

Figure 1. Nanoparticle synthesis and characterization

(A) Schema of Dox encapsulated within the HAuNS. (B) UV-vis absorption profile of Dox, HAuNS, and Dox-HAuNS. Note that the maximum absorption wavelength of Dox is at 490 nm, while HAuNS is at 808 nm. (C) TEM images of the HAuNS. (D) Radio-labeling stability of ^{64}Cu Dox-HAuNS at 24 hours

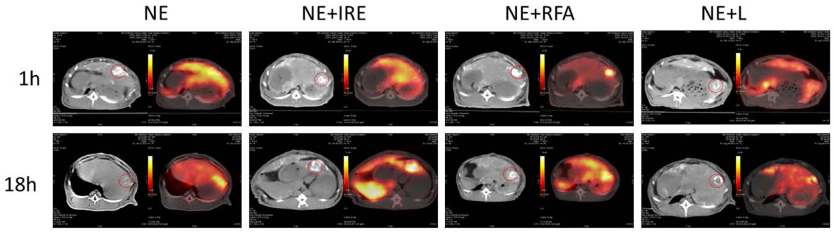

Figure 2. PET/CT demonstrates the distribution of ^{64}Cu-labeled-Dox-HAuNS after treatment at two time points

Non-contrast enhanced CT imaging demonstrates the high density lipiodol oil in and around the tumors (circled) and to a lesser extent, in the normal liver parenchyma in all animals. In the corresponding PET images, focal localization of the nanoparticles is most pronounced on early imaging after NE+RFA. However, the delayed PET images demonstrate that after 18-hours, all treatment modalities had evidence of increased localization of the ^{64}Cu-labeled-Dox-HAuNS in the tumor and the calculated tumor-to-normal liver uptake ratios were elevated.

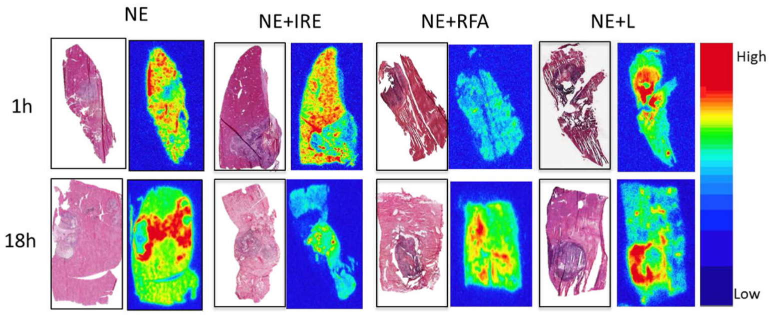

Figure 3. Autoradiographs demonstrate nanoparticle distribution in the tumor as compared with hematoxylin and eosin stained slides after treatment

The red areas on the autoradiographs represent the “hottest” areas with the highest concentration of accumulated nanoparticles (^{64}Cu-labeled-Dox-HAuNS). In the NE and NE +RFA animals, the distribution of the ^{64}Cu-labeled-Dox-HAuNS is predominantly around the tumor. In the NE+IRE and NE+LITT animals, the distribution of the ^{64}Cu-labeled-Dox-HAuNS is both in and around the tumor.

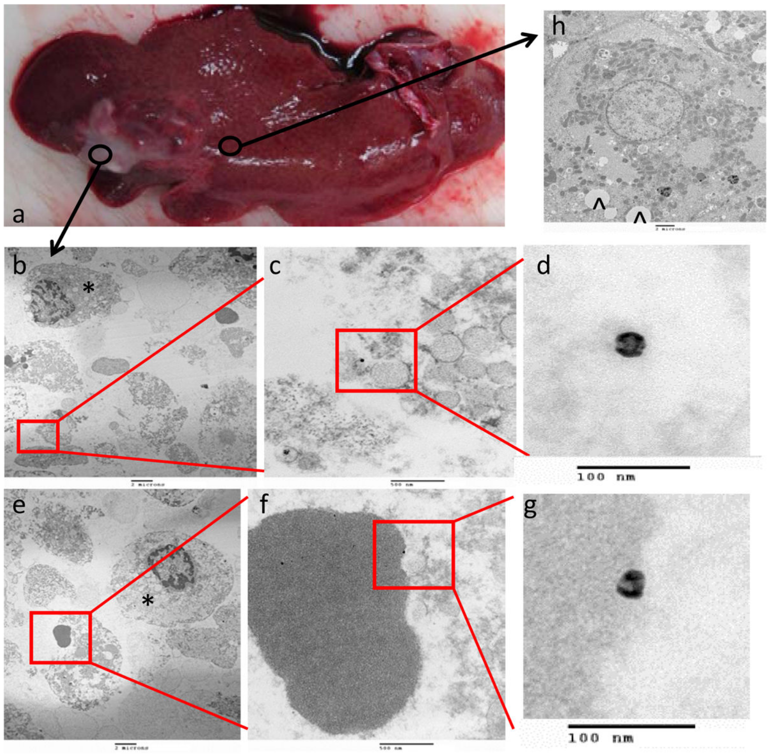

Figure 4. TEM localization of ^{64}Cu-labeled-Dox-HAuNS after nanoembolization

The gross specimen consisting of tumor and surrounding normal liver (a) demonstrates the areas from which the samples were taken. Images from samples taken from the tumor are presented in increasing magnification (b,e: 5000x; c,f: 50000x; d,g: 200000x). Most of the nanoparticles (^{64}Cu-labeled-Dox-HAuNS) were seen in the interstitial space (b-d) in between tumor cells (*) or in blood vessels. A single erythrocyte with an attached nanoparticle is shown (e-g). An image from normal liver is shown in (h) and demonstrates the presence of “fatty” lobules (^) inside of the cell. These likely represent droplets of the lipiodol oil used during nanoembolization. The nanoparticles retain their spherical shape.

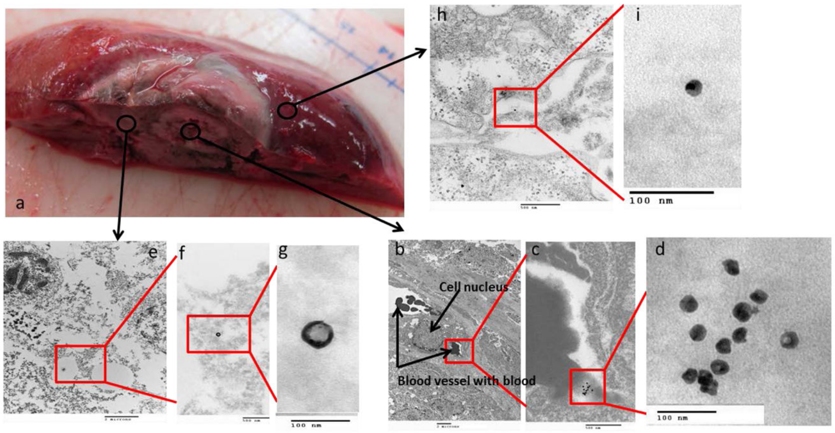

Figure 5. TEM localization of ^{64}Cu-labeled-Dox-HAuNS after nanoembolization+RFA

The gross specimen consisting of tumor, and surrounding ablated and peri-tumoral, non-ablated liver (a) demonstrates the areas from which the samples were taken. Images obtained from a representative sample taken from the tumor are presented in increasing magnification (b: 5000x; c: 50000x; d: 200000x). The nanoparticles (^{64}Cu-labeled-Dox-HAuNS) were seen inside the blood vessels (b,c) but not inside the tumor cell (the cell nucleus is annotated). The highest magnification image (d) demonstrates that the nanoparticles have retained their spherical shape. Images obtained from a representative sample taken from the ablation zone are presented in increasing magnification (e: 10000x; f: 50000x; g: 200000x). The ^{64}Cu-labeled-Dox-HAuNS were predominantly noted to be in between cells in the interstitial space; however, the ablated tissue had been thermally damaged making it difficult to discern the exact location of the nanoparticles. The highest magnification image (g) demonstrates the spherical shape of the nanoparticle. Images obtained from a representative sample taken from peri-tumoral, non-ablated liver are presented in increasing magnification (h: 50000x; i: 200000x) and demonstrate a spherical nanoparticle (i) located in the interstitial space between two cells, whose membranes are denoted by (*)'s (h).

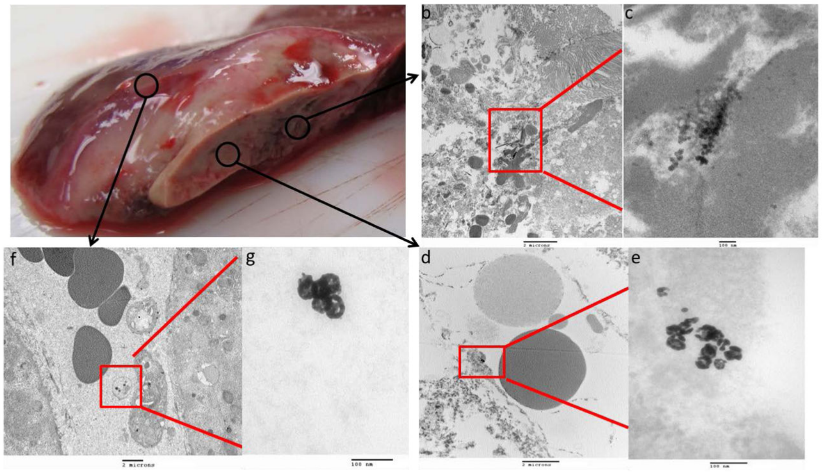

Figure 6. TEM localization of ^{64}Cu-labeled-Dox-HAuNS after nanoembolization+LITT

The gross specimen consisting of tumor, and surrounding ablated and peri-tumoral, non-ablated liver (a) demonstrates the areas from which the samples were taken. Images obtained from a representative sample taken from the tumor are presented in increasing magnification (b: 10000x; c: 100000x). The tissues sampled were thermally damaged but it appeared that the nanoparticles (^{64}Cu-labeled-Dox-HAuNS) were seen outside the tumor cells. The highest magnification image (c) demonstrates that the nanoparticles are not all spherical with some demonstrating collapse of the nanoshell. Images obtained from a representative sample taken from the ablation zone are presented in increasing magnification (d: 10000x; e: 200000x). The ^{64}Cu-labeled-Dox-HAuNS were predominantly seen in the interstitial space (d) and structural deformity is again noted (e). The nanoparticles demonstrating a collapse of the shell also appear smaller. Images obtained from a representative sample taken from peri-tumoral, non-ablated liver are presented in increasing magnification (f: 5000x; g: 200000x) and demonstrate the extracellular location of the nanoparticles (f). Unlike the ^{64}Cu-labeled-Dox-HAuNS in the tumor and ablation zone, nanoparticles found in peri-tumoral, non-ablated liver retained their spherical shape.

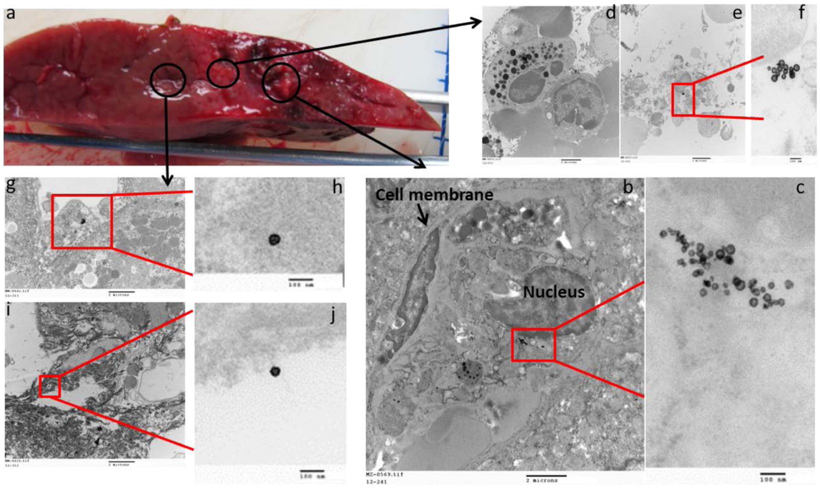

Figure 7. TEM localization of ^{64}Cu-labeled-Dox-HAuNS after nanoembolization+IRE

The gross specimen consisting of tumor, and surrounding ablated and peri-tumoral, non-ablated liver (a) demonstrates the areas from which the samples were taken. Images obtained from a representative sample taken from the tumor are presented in increasing magnification (b: 10000x; c: 100000x). The cell membrane and nucleus are annotated. The nanoparticles (^{64}Cu-labeled-Dox-HAuNS) were seen inside the tumor cell adjacent to the nucleus. The highest magnification image (c) demonstrates that the nanoparticles have retained their spherical shape. Images obtained from a representative sample taken from the ablation zone are presented in increasing magnification (d,e: 10000x; f: 100000x). The intracellular black dots (d) seen in the cells in the ablation zone represent lysosomes and are seen in increased numbers. The spherical ^{64}Cu-labeled-Dox-HAuNS were predominantly noted to be inside the cells (e,f). Images obtained from a representative sample taken from peri-tumoral, non-ablated liver are presented in increasing magnification (g,i: 10000x; h,i: 100000x) and demonstrate the spherical nanoparticles to be located both inside cells (g,h) and in between cells in the interstitial space (I,j).

Table 1

Gross pathology and PET/CT specific uptake value measurements

	Tumor Volume (cm^3)		**Ablation Zone Volume (cm^3)**		**SUV of Tumor ± Std**		**SUV of Normal Liver ± Std**		**SUV Ratio (Tumor/Liver)**	
	1hr	**18h**	**1hr**	**18h**	**1hr**	**18h**	**1hr**	**18h**	**1hr**	**18h**
Nanoembolization	0.63	0.71	N/A	N/A	13.9±2.3	14.1±2.5	12.8±2.5	8.2±0.51	1.1	1.7
Nanoembolization+RFA	1.26	0.61	4.4	10.1	21.5±6.5	13.6±1.4	4.6±0.17	9.7±0.65	4.7	1.4
Nanoembolization+IRE	0.58	1.13	3.46	21.4	12.6±1.4	12.3±2.5	15.5±0.95	6.3±0.58	0.81	2.0
Nanoembolization+L	0.45	0.63	1.01	1.31	4.8±0.46	17.9±1.9	2.2±0.29	11.8±0.73	2.0	1.5

Notes: Volume of tumor and ablation zone calculated using the formula for an ellipsoid where Volume = $4/3\pi * abc$ where $\pi = 3.14159$; a = radius of width of tumor or tumor+ablated tissue (for ablation zone calculation); b = radius of length of tumor or tumor+ablated tissue (for ablation zone calculation); and c = radius of depth of tumor or tumor+ablated tissue (for ablation zone calculation).

Abbreviations: cm^3, cubic centimeters; SUV, specific uptake value; Std, standard deviation; RFA, radiofrequency ablation; IRE, irreversible electroporation; L, laser; N/A, not applicable.